Monthly Notices
of the
ROYAL ASTRONOMICAL SOCIETY

Mon. Not. R. Astron. Soc. **415,** 2485–2494 (2011) doi:10.1111/j.1365-2966.2011.18872.x

SGR 1806−20 distance and dust properties in molecular clouds by analysis of flare X-ray echoes

Gilad Svirski,[1⋆] Ehud Nakar[1] and Eran O. Ofek[2]†

[1]*Raymond and Beverly Sackler School of Physics & Astronomy, Tel Aviv University, Tel Aviv 69978, Israel*
[2]*Division of Physics, Mathematics and Astronomy, California Institute of Technology, Pasadena, CA 91125, USA*

Accepted 2011 April 7. Received 2011 April 6; in original form 2011 February 23

ABSTRACT

The soft gamma repeater SGR 1806−20 is most famous for its giant flare from 2004, which yielded the highest gamma-ray flux ever observed on Earth. The flare emphasized the importance of determining the distance to the SGR, thus revealing the flare's energy output, with implications on SGRs energy budget and giant flare rates. We analyse X-ray scattering echoes observed by *Swift*/X-Ray Telescope (XRT) following the 2006 August 6 intermediate burst of SGR 1806−20. Assuming positions and opacities of the molecular clouds along the line of sight from previous works, we derive direct constraints on the distance to SGR 1806−20, setting a lower limit of 9.4 kpc and an upper limit of 18.6 kpc (90 per cent confidence), compared with a 6–15 kpc distance range by previous works. This distance range matches an energy output of $\approx 10^{46}$ erg for the 2004 giant flare. We further use, for the first time, the X-ray echoes in order to study the dust properties in molecular clouds. Analysing the temporal evolution of the observed flux using a dust-scattering model, which assumes a power-law size distribution of the dust grains, we obtain a power-law index of $-3.3^{+0.6}_{-0.7}$ (1σ) and a lower limit of 0.1 μm (2σ) on the dust maximal grain size, both conforming to measured dust properties in the diffused interstellar medium (ISM). We advocate future burst follow-up observations with *Swift*, *Chandra* and the planned *NuSTAR* telescopes, as means of obtaining much superior results from such an analysis.

Key words: ISM: clouds – dust, extinction – gamma-rays: general – X-rays: individual: SGR 1806−20.

1 INTRODUCTION

Soft gamma repeaters (SGRs) are objects emitting soft gamma-ray and hard X-ray bursts at irregular intervals, as well as a persistent X-ray emission (for a review see Woods & Thompson 2006 and references therein). Bursts are typically short (∼0.1 s) and are gathered within active periods that last between a few weeks and several months, followed by years of quiescence (Kouveliotou 1998). Bursts are commonly classified according to their peak luminosity, from the most common flares reaching 10^{41-42} erg s^{-1}, up to the rare 'giant' flares reaching $\sim 10^{46}$ erg s^{-1}. SGRs are believed to be magnetars – neutron stars with a surface magnetic field of $\sim 10^{15}$ G, which serves as the energy source of the bursts and the persistent emission (Duncan & Thompson 1992; Paczynski 1992; Kouveliotou et al. 1998).

SGR 1806−20, lying in the direction of the Galactic Centre behind a veil of 15–30 mag of optical extinction (Corbel & Eikenberry 2004, hereafter CE04), is one of a handful of known SGRs. Its resume includes the first SGR to be observed, on 1979 January 7 (originally classified as a gamma-ray burst, Mazets & Golenetskii 1981) and the subject of the first SGR spin-down rate measurement (Kouveliotou et al. 1998) – a major milestone in the acceptance of the magnetar hypothesis. Yet it is most famous for producing the most energetic giant flare observed to date; on 2004 December 27 it emitted a 0.1-s flare with an estimated total energy of $2\text{–}5 \times 10^{46} (\frac{d}{15\,\mathrm{kpc}})^2$ erg, where d is the distance to the SGR (Hurley et al. 2005; Palmer et al. 2005). The emitted energy in this event is evaluated as 100 times higher than the next most energetic SGR recorded event (assuming $d = 15$ kpc).

An energy of $E \sim 10^{46}$ erg is at odds with some of the observations. First, a naive rate of $\frac{1}{150}$ yr^{-1} flares with similar energy per SGR[1] is ruled out by failure to observe corresponding population of extragalactic SGRs (detectable to ∼30 Mpc, Palmer et al. 2005; Nakar et al. 2006). Moreover, even a rate of a single giant

⋆E-mail: giladsv@gmail.com
†Einstein Fellow.

[1] Based on a single $E \approx 10^{46}$ erg event within 30 yr of observing ∼5 SGRs, as of 2004.

flare per SGR life-span, within 2σ of the observed rate obtained by a careful statistical treatment, has only marginal agreement with observed extragalactic rates (Ofek 2007). Second, the surface magnetic field corresponding to observed properties of SGRs (e.g. spin-down rate) is $B \approx 10^{15}$ G, matching an external magnetic energy of $\sim 10^{47}$ erg, comparable to the energy output of a single giant flare. Since the source of both the energy reservoir powering giant flares and the reservoir responsible for the persistent emission is thought to be the surface magnetic field of the SGR, one might expect a significant transformation in the observed spectral and temporal emission parameters of SGR 1806−20 following the giant flare. This expectation is not met by observations[2] (Esposito et al. 2007; Woods et al. 2007). A possible explanation for both the discrepancies in rates and the unchanged emission features is a distance shorter than the commonly assumed 15 kpc to SGR 1806−20, matching a less energetic flare output.

Employing different approaches, several papers in recent years suggest distance ranges within 6–15 kpc to SGR 1806−20. The emerging factor of nearly 3 in the SGR's distance estimates translates into nearly an order of magnitude difference in its emitted energy. CE04 used CO emission lines and NH_3 absorption features from molecular clouds along the line of sight to find the clouds' radial velocities, inferring two possible locations per cloud, one in front of the Galactic Centre and the other behind it. Accounting for the optical extinction of the star powering the nebula LBV 1806−20, they determined a distance of $15.1^{+1.8}_{-1.3}$ kpc (2σ) to the cluster containing LBV 1806−20. They associated SGR 1806−20 with this cluster due to its angular proximity of 12 arcsec to LBV 1806−20 and the match between SGR 1806−20 X-ray absorption and the infrared (IR) extinction towards the cluster members. Figer, Najarro & Kudritzki (2004) measured radial velocities using absorption lines from LBV 1806−20 and nearby stars, which translated into a distance of 11.8 kpc. Bibby et al. (2008) spectroscopically classified several stars which were identified as members of the cluster of LBV 1806−20 by CE04 and Figer et al. (2005). Based on their absolute magnitude calibration and near-IR photometry, as well as isochrones fit to the cluster's age, they obtained a cluster distance of $8.7^{+1.8}_{-1.5}$ kpc. As opposed to the above associative distance estimations, Cameron et al. (2005) gave a more direct estimate. They identified the decaying bright radio afterglow of the 2004 December giant flare a week after the burst. Based on the absorption features of intervening interstellar neutral hydrogen clouds, they constrained SGR 1806−20 distance to within 6.4–9.8 kpc. McClure-Griffiths & Gaensler (2005) accepted the lower limit of ∼6 kpc but rejected their upper limit, disqualifying the association of the absorption feature used to set this limit with SGR 1806−20.

We present a new direct estimate of the distance to SGR 1806−20 based on dust-scattered X-ray observations, from which we also extract properties of the dust along the line of sight. The scattering of X-rays from dust grains in the interstellar medium (ISM) was first considered by Overbeck (1965). For an X-ray source with a varying intensity (e.g. a short burst), if the dust spatial distribution is known, one can use the time delay between the direct signal and the scattered signal to constrain the distance to the X-ray source (Trümper & Schönfelder 1973). This was first applied for constraining the distance to the X-ray binary Cyg X-3 (Predehl et al. 2000).

Analysis of X-ray haloes around Galactic and extragalactic sources have been used to constrain the properties of dust grains in the ISM (Mauche & Gorenstein 1986; Predehl & Schmitt 1995), with results conforming to the dust model by Mathis, Rumpl & Nordsieck (1977). Such analyses exploit the dependence of the scattering cross-section on the grain properties as well as the dependence of the halo radial profile on the positions of the scattering grains along the line of sight.

In the case of both a short burst and a thin dust scatterer, the halo is replaced by a ring, radius of which increases with time. Measuring the expansion rate of such observed rings from gamma-ray bursts (GRBs) has been used to derive distances to Galactic dust clouds (Vianello, Tiengo & Mereghetti 2007) as well as the time of the original burst (Feng & Fox 2010). Tiengo et al. (2010) combined observations by both *Swift*/X-Ray Telescope (XRT) and *XMM–Newton*/EPIC of rings following bursts of the anomalous X-ray pulsar 1E1547.0–5408, and used several different models for the dust composition and grain size distribution to fit the intensity decay of each ring as a function of time and energy, in order to obtain constraints on the distance to the X-ray source. They concluded that in the absence of independent constraints on the distance of the source or the scatterer, their analysis is highly sensitive to the size of the largest dust grains, as reflected by each of the models used. A dust-scattered halo surrounding an SGR was first reported by Kouveliotou et al. (2001) for SGR 1900+14, with data quality not good enough for further analysis.

The dust along the line of sight to SGR 1806−20 is concentrated within molecular clouds (e.g. CE04). As opposed to the diffused ISM, where dust properties are efficiently probed using UV and longer wavelengths, the dust in cores of molecular clouds is not easily accessible due to the clouds' high optical depth at these wavelength. Moreover, observational evidence (Carrasco, Strom & Strom 1973; Jura 1980; Goldsmith, Bergin & Lis 1997; Stepnik et al. 2003; Chiar et al. 2007; Winston et al. 2007; Schnee et al. 2008; Butler & Tan 2009) and theoretical considerations (e.g. Ossenkopf 1993; Weidenschilling & Ruzmaikina 1994; Ormel et al. 2009) indicate that the high density in molecular clouds leads to grain coagulation that alters the dust grain size distribution from the one observed in the diffused ISM. Since molecular clouds are optically thin to hard X-rays, small-angle X-ray scattering provides a unique tool to directly probe grain size distribution at their cores. Despite this virtue, X-rays have not been used yet to probe dust properties in molecular clouds. Here we seize the opportunity to employ, for the first time, X-ray echoes for this purpose.

On 2006 August 6, an intermediate burst of SGR 1806−20 was observed (Hurley et al. 2006a,b). Anticipating delayed dust-scattered echoes, *Swift*/XRT took a dozen observations during the two weeks following the burst. A preliminary analysis of the first two observations by Goad et al. (2006) revealed an expanding halo due to dust scattering. We re-analyse *Swift* observations, finding the halo flux profile of each observation. Assuming properties of molecular clouds along the line of sight to SGR 1806−20 as reported in CE04, we use the observation profiles to constrain the distance to SGR 1806−20. We then assume, instead of the CE04 dust distribution, a single predominant dust screen along the line of sight and a power-law distribution for the dust grain size, and use the observations to constrain the grain size distribution within the intervening molecular cloud that dominates the scattering.

This paper is organized as follows. Observations are described in Section 2. Section 3 reviews the dust-scattering model we use in

[2] These works do report changes in the temporal characteristics of the SGR following the giant flare, suggesting reorganization of the magnetic field. Similar reports followed the giant flare of SGR 1900+14, e.g. Göğüş et al. (2004). However, the loss of a significant portion of the total energy reservoir seems to justify a more dramatic change.

Table 1. *Swift*/XRT observations used in the analysis. Times are given in hours, start and end times are relative to the burst trigger. Total duration is the time elapsed between the start and end time while exposure time is the net time for which the detector was actively collecting signal.

Obs. ID	Start time (h)	End time (h)	Total duration (h)	Exposure time (h)
00035315002	30.50	31.17	0.66	0.66
00035315003	82.22	104.81	22.59	3.89
00035315004	112.94	129.17	16.23	1.89
00035315005	141.93	153.29	11.36	1.88

our analyses, which are then presented in Section 4. In Section 4.1 we assume that the distance of the scattering clouds is known from CE04 and constrain the distance to SGR 1806−20. In Section 4.2 we relax our assumptions regarding the distance to the scattering clouds and study the properties of the scattering dust. In Section 5 we discuss the implications of our analyses for future observations, and we draw our conclusions in Section 6.

2 OBSERVATIONS

SGR 1806−20 intermediate burst of 2006 August 6 was first reported by Hurley et al. (2006a,b). It comprised six separate bursts over ≈120 s, with the dominant one lasting for ≈30 s and characterized by a measured fluence of 2.4×10^{-4} erg cm^{-2} and an optically thin thermal bremsstrahlung (OTTB) spectrum of $kT = 20$ keV within the Konus–Wind range of 20–200 keV (Golenetskii et al. 2006). Following this report, *Swift*/XRT took 12 observations in the Photon Count mode, starting 30 h after the burst and ending 14 d later, corresponding to observation ID 00035315002−00035315013. For our analysis we used the four earliest observations (see Table 1; for the first and second observations, see Fig. 1). The other observations did not show a significant signal and were only used implicitly for background consistency check. *Swift*/XRT is sensitive to photons in the energy range of 0.2–10 keV, and the dust-scattered signal in the observations is only evident in the range of 2.5–8.5 keV. Below this range the optical depth is larger than unity and the assumption of a single scattering does not hold. In order to allow energy-dependent analysis without diluting the signal too much, we split each observation data into two energy bands: 2.5–4.5 and 4.5–8.5 keV. We created exposure maps for each observation and each energy band with the FTOOLS task XRTEXPOMAP, to correct for the vignetting, the dead detector areas and the excluded regions. For each observation we extracted a radial profile centred at the position of SGR 1806−20 given by the FTOOLS task XRTCENTROID. A radial binwidth of 8 pixels (19) arcsec was chosen so that it overlaps with the average *Swift*/XRT point spread function (PSF) of ≅20 arcsec (half power diameter, Burrows et al. 2005). We estimated the background photon count per energy band for each observation by taking the average photon count at a radial distance where no dust-scattered signal is expected and by adjusting for the area of each radial bin and for its average exposure time derived from the exposure map. The background thus measured agrees across all the 12 observations with a photon count $C = 1.40 \pm 0.13 \times 10^{-1}$ photons s^{-1} for the 2.5–4.5 keV band and $C = 9.57 \pm 1.20 \times 10^{-2}$ photons s^{-1} for the 4.5–8.5 keV band over the XRT detection area.

The profile cannot be explained by the scattered signal and the background alone, and is found to consist of a third component – a fading halo around the SGR. This halo is wider than the central source PSF and therefore it also contains one or more of the following contributions: an integration over dust-scattered rings that have originated from fading post-burst source emission at times between the burst and the observation; dust-scattered rings unresolved from the source due to dust clouds adjacent to the source; and multiple scattering. Because of our lack of knowledge of the post-burst source luminosity as a function of time and confined by the XRT resolution, we model this halo as a two parameters King function $C(1 + (\frac{r}{30})^2)^{-\beta}$. This component has no significant effect on our background evaluations since the King function is negligible at the radial distance used for background measurement.

3 DUST-SCATTERED X-RAY RINGS

An SGR flare can be considered a special case of a varying source, where the flare is approximately a delta function in time, and the result of an intervening dust screen is a ring expanding with time. For small scattering angles and a single scattering screen, geometry dictates

$$\theta(t) \cong \left[\frac{2c}{d}\frac{(1-x)}{x}t\right]^{1/2}, \quad (1)$$

where $\theta(t)$ is the measured ring angle with respect to the line of sight, d is the source distance, x is the screen's location expressed as a fraction of d and t is the time passed since the direct flare observation.

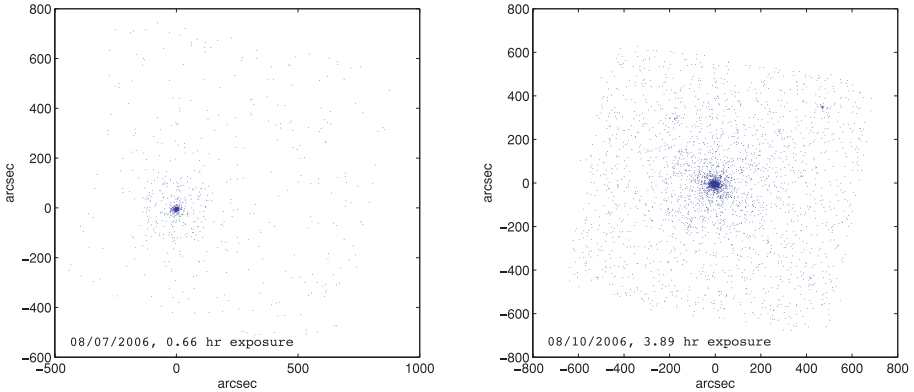

Figure 1. The dust rings seen in the first (left, ≈31 h after the burst) and second (right, ≈90 h after the burst) *Swift*/XRT observations, (energy range 2.5–8.5 keV).

We fit the observations to a model based on Smith & Dwek (1998), with differential scattering cross-section as described in Rivera-Ingraham & van Kerkwijk (2010). The original model calculates the halo observed by the scattering of X-rays from a persistent source over a continuous distribution of intervening dust. We are interested in the rings produced by the scattering of an impulsive emission over one or more molecular clouds, namely a discrete distribution of intervening dust. Our configuration is simpler and it allows us to derive an analytic solution. We therefore modify the original derivation by Smith & Dwek (1998) to obtain an analytic expression for the flux in a ring produced by the scattering of a flare on a single thin dust screen, i.e. the scattered flux observed at an angular distance $\theta_{\rm obs}(t)$ from the central source, as a function of photon energy. The modification is straightforward and we therefore do not repeat the derivation of Smith & Dwek (1998) here, and just highlight the modifications. Keeping the original notations, we replace the dust distribution along the line of sight with the dust column density across the scattering screen, $N_{\rm dust}$, and the dust grain size distribution with $N_{\rm a}$, such that $N_{\rm dust} = \int N_{\rm a}{\rm d}a$, where a is the radius of the dust grain. We further replace the flux reaching the scatterer, used in the original derivation, by the flare's total fluence reaching it. In addition, the solid angle which the scattered observed signal occupies, ${\rm d}\Omega'$, is $2\pi\theta(t){\rm d}\theta$ where ${\rm d}\theta$ is the change in the observed angle during the observation time ${\rm d}t$. Using equation (1) we find ${\rm d}\Omega' = g(x){\rm d}t$, where $g(x) = \frac{2\pi c}{d}\frac{(1-x)}{x}$. The observed scattered flux per photon energy E, F_E (energy observed in a ring per photons of energy E per unit area per unit time ${\rm d}t$) is thus

$$F_E\left(\theta_{\rm obs}[t]\right) = S_E \frac{g(x)}{(1-x)^2}\int_{a_{\rm min}}^{a_{\rm max}} N_{\rm a}\left(\frac{{\rm d}\sigma}{{\rm d}\Omega}\right){\rm d}a, \tag{2}$$

where S_E is the flare's direct (versus scattered) observed fluence per photon energy E and ${\rm d}\sigma(E, a, \theta_{\rm scat})/{\rm d}\Omega$ is the differential scattering cross-section of an X-ray with energy E by a dust grain with radius a at an angle $\theta_{\rm scat}$.

As the scattering angles are small, we substitute $\theta_{\rm scat} = \theta_{\rm obs}/(1-x)$. For the dust grain size distribution we assume a power law, $N_{\rm a} = Aa^q$, where $a_{\rm min} \le a \le a_{\rm max}$ (Mathis et al. 1977). For the differential cross-section we use the Gaussian approximation of the Rayleigh–Gans theory, valid for small scattering angles and energies above 1 keV, following van de Hulst (1957):

$$\frac{{\rm d}\sigma(E, a, \theta_{\rm scat})}{{\rm d}\Omega} \cong C_{\rm dust}a^6 \exp\left(-\frac{\theta_{\rm scat}^2}{2\tilde{\theta}_{\rm scat}^2}\right), \tag{3}$$

where $C_{\rm dust}$ depends on the dust component's atomic charge, mass number, density and scattering factor, while $\tilde{\theta}_{\rm scat}$ is given by Mauche & Gorenstein (1986):

$$\tilde{\theta}_{\rm scat}(a, E) = 10.4\frac{1}{(E/1\,{\rm keV})({\rm a}/0.1\,\mu{\rm m})}\,{\rm arcmin}. \tag{4}$$

Inserting the cross-section and dust grain size distribution, we obtain

$$F_E(\theta_{\rm obs}, q, \hat{a}_{\rm max}, \hat{a}_{\rm min}) = B_E\int_{\hat{a}_{\rm min}}^{\hat{a}_{\rm max}} \hat{a}^{q+6}\exp\left\{-\frac{1}{2}\left(\frac{\theta_{\rm obs}}{10.4'}\right)^2\left(\frac{\hat{a}}{0.1\,\mu{\rm m}}\right)^2\left(\frac{E}{1\,{\rm keV}}\right)^2\right\}{\rm d}\hat{a}, \tag{5}$$

where $\hat{a} \equiv \frac{a}{1-x}$, and

$$B_E = S_E C_{\rm dust}A\frac{2\pi c}{d}(1-x)^{q+6}/x. \tag{6}$$

The differential cross-section (equation 3) implies that a dust grain of size a scatters effectively below a characteristic angle $\tilde{\theta}(a)$, above which the differential cross-section decays rapidly. Thus, for a grain size distribution more gradual than a^{-7}, regardless of its exact form, the scattering at an angle of $\theta_{\rm scat}$ is dominated by the grain size matching equation (4):

$$a_{\rm scat}(\theta_{\rm scat}, E) \approx \frac{0.1}{(E/1\,{\rm keV})(\theta_{\rm scat}/10.4\,{\rm arcmin})}\,\mu{\rm m}. \tag{7}$$

The observed scattered flux can then be approximated as $F_E(\theta) \propto N_{\rm a_{scat}}a_{\rm scat}^7$. If the grain size distribution is limited to the range $a_{\rm min} \le a \le a_{\rm max}$ then at small angles (early time) $a_{\rm scat} > a_{\rm max}$ and the scattering is dominated by the largest grains, namely it is constant in angle (time) and $F_E \propto N_{a_{\rm max}}a_{\rm max}^7$. At large angles (late time) when $a_{\rm scat} < a_{\rm min}$ the scattering is dominated by the Gaussian tail of the smallest grains cross-section, and the flux falls exponentially. Therefore, defining $\tilde{\theta} = (1-x)\tilde{\theta}_{\rm scat}$, equation (5) can be approximated as

$$F_E(\theta) \propto \begin{cases} {\rm const} & \theta_{\rm obs} \ll \tilde{\theta}(a_{\rm max}) \\ \theta_{\rm obs}^{-(q+7)} & \tilde{\theta}(a_{\rm max}) \ll \theta_{\rm obs} \ll \tilde{\theta}(a_{\rm min}) \\ \exp\left[-\frac{\theta_{\rm obs}^2}{\tilde{\theta}^2(a_{\rm min})}\right] & \theta_{\rm obs} \gg \tilde{\theta}(a_{\rm min}). \end{cases} \tag{8}$$

It is useful to express this approximation in terms of the flux dependence on time, using equation (1):

$$F_E(t) \propto \begin{cases} {\rm const} & t \ll \tilde{t}(a_{\rm max}) \\ t^{-(q+7)/2} & \tilde{t}(a_{\rm max}) \ll t \ll \tilde{t}(a_{\rm min}) \\ \exp\left[-\frac{t}{\tilde{t}(a_{\rm min})}\right] & t \gg \tilde{t}(a_{\rm min}), \end{cases} \tag{9}$$

where $\tilde{t}(a, E) = \frac{{\rm d}x}{2c(1-x)}\tilde{\theta}^2(a, E)$. These expressions describe three flux regimes: (i) a constant set by scattering over the largest grains; (ii) a power-law decay where the size of the grains that dominate the scattering vary with time; and (iii) an exponential decay set by the scattering cross-section of the smallest grains. Therefore, observing the evolution of F_E with time is a direct probe of the dust grain size distribution. $a_{\rm max}$ is probed by observations covering the time of transition between the constant and the power-law regime, while the index q is obtained by power-law regime observations. Probing $a_{\rm min}$ requires a burst bright enough for the scattered signal to overcome the background at the low end of the power-law regime.

We note that equation (10) in Draine (2003), which is an analytical approximation for the differential scattering cross-section describing his model of X-ray scattering by dust, can be closely matched by the above scattering model by choosing $a_{\rm max} = 0.33\,\mu{\rm m}$ and $q = -3$, which are typical values for ISM dust.

4 ANALYSIS AND RESULTS

To achieve our two objectives – constraining the distance to SGR 1806−20 and the properties of the dust in the intervening molecular clouds – we take two different approaches in analysing the XRT observations. First (Section 4.1), we assume positions and visual extinctions of molecular clouds along the line of sight based on CE04 in order to get an estimate of the distance to SGR 1806−20. We test the dependence of this analysis on a dust-scattering model and find it to be negligible. Therefore our conclusion is based on the accuracy of CE04 clouds' distribution, and is mainly limited by the XRT resolution and sensitivity.

In the second subsection (Section 4.2) we relax our assumptions regarding the distance to the scattering clouds, and motivated by observations we assume a single predominant scattering screen. We

keep the location of this screen a free parameter, and use equation (5) to put simultaneous constraints on both the dust screen location and the dust properties, using a full data set including both spectral and temporal flux evolution. The results of this analysis are limited mainly by the delay of the first observation and by the sensitivity of the XRT detector.

4.1 Distance estimate based on known molecular clouds along the line of sight

Equation 2 expresses the observed scattered flux as a function of (1) the scatterer's location relative to the source (i.e. x) and (2) properties of the scattering dust. Therefore, if the location of the scatterers and the properties of the dust are known, one can extract the distance to the source. In fact, as we show here, it is enough to know the location of the dust screens along the line of sight and their dust column densities to put strong constraints on the source distance, even if the grain size distribution, N_a, is not well known. CE04 provide the locations of the scattering clouds along the line of sight to SGR 1806−20, as well as their optical extinction A_V, which indicate on their dust column densities. Using this data we calculate the scattered flux radial profile for different locations of the source. We then compare these 'synthetic' profiles with the observed profiles and use the best-fitting profile to infer the distance.

Table 2 lists properties of the molecular clouds along the line of sight, adapted from table 1 of CE04. Following radial velocity measurements, each cloud has two distance solutions and was therefore attributed with a near distance and a far distance, as well as the optical extinction A_V. For eight clouds CE04 ruled out one of these distances due to additional considerations. We assume that the A_V given for each cloud is proportional to its share of the clouds' total dust column density (i.e. $A_V \propto A$ in equation 6). Equipped with the clouds' positions and dust shares, we assume a single dust grain size distribution across all clouds and set $a_{\rm max} = 0.3\,\mu$m, $a_{\rm min} = 0\,\mu$m, $q = -3$. Assuming a source distance we use equations (1) and (5) to calculate the scattered flux from each of the intervening clouds and construct a synthetic flux radial profile at any given time and energy band. In order to compare the profile calculated using equations (1) and (5) to the observations, it must be smeared by the PSF, the exposure duration and the width of the scattering clouds. We therefore introduce the *Swift*/XRT PSF (Moretti et al. 2005), and we account for the observations' actual exposure durations to widen the profile beyond the PSF effect. Assuming a typical molecular cloud width of ∼100 pc, the consequent smear is negligible. We repeat this calculation for an SGR 1806−20 distance that vary in the range 5–25 kpc with a 0.1-kpc resolution. Note that the synthetic profiles are calculated up to a normalization factor per energy band, accounting for the unknown direct fluence from the source S_E, as well as both $C_{\rm dust}$ and the constant of proportionality in $A \propto A_V$.

Table 2. Molecular clouds along the line of sight to LBV 1806−20, taken from CE04. The bottom three clouds, lacking unambiguous distance determinations, are quoted with both near and far distances (1σ errors). CE04 do not determine whether the three last clouds in this table are in front or behind the Galactic Centre, allowing two distances to each cloud. In the text we refer to all the three clouds being in front of the Galactic Centre as the 'near' configuration, while all three clouds being at their far distance is the 'far' configuration.

Name	A_V (mag)	Distance (kpc)
MC-16	8.6 ± 1.7	4.5 ± 0.3
MC4	3.9 ± 0.8	0.2 ± 0.5
MC13A	10.0 ± 2.0	15.1 ± 0.9
MC13B	3.0 ± 0.6	4.5 ± 0.3
MC24	5.6 ± 1.1	3.0 ± 0.5
MC30	0.8 ± 0.2	3.5 ± 0.35
MC38	1.1 ± 0.2	4.2 ± 0.3
MC44	1.6 ± 0.3	4.5 ± 0.3
MC73	6.0 ± 1.2	$5.7/11.0 \pm 0.15$
MC87	1.4 ± 0.3	$6.1/10.6 \pm 0.15$
MC94	0.5 ± 0.1	$6.2/10.5 \pm 0.15$

The actual observed signal contains two additional features beyond the dust-scattered flux, and we therefore model the observed radial flux profile as a sum of the three following contributions: (a) the synthetic profile of the dust-scattered signal, calculated as described above; (b) the measured background profile; and (c) the halo around the SGR described in Section 2. Therefore, our model contains the following free parameters: the halo amplitude and power law per observed profile, the normalization factor of the scattered signal per energy band, and the SGR distance.

We compare this model with the observed profiles from the first two epochs in Table 1, where the observed dust-scattered ring is most evident, with each epoch split into two energy bands. For each distance we use a χ^2 fit to find the halo amplitude and power law per observed profile, and the normalization factor per energy band. We then calculate χ^2 as a function of distance and choose the distance yielding the overall minimal χ^2 as the best-fitting distance.

Three of the clouds lack an unambiguous distance determination and have instead both a near and a far distance estimate, similarly for all three clouds. To account for this uncertainty we prepare two sets of scattered signal profiles as a function of SGR distance, one with all the three clouds set at their 'near' position, and the other with all the three at their 'far' position, and repeat the above procedure for both the sets. We verify that other combinations, where some of the clouds are at an opposite location, result in intermediate SGR locations and therefore the 'far' and 'near' configurations bracket the constraints on the location of SGR 1806−20.

In order to estimate the distance error we use Monte Carlo simulations (following the prescription in Press, Flannery & Teukolsky 1986). For each Monte Carlo realization we generate a pseudo-binned radial profile by drawing the 'observed' radial bins photon counts from a Poisson distribution around the best-fitting radial profile. We further prepare synthetic scattered profiles per SGR distance by drawing the clouds' positions[3] and optical extinctions (from Table 2), assuming an approximately normal distribution for both. We repeat the fitting procedure described above for each of the 10 000 Monte Carlo realizations and thus obtain the probability distribution of the SGR distance (see Fig. 2).

[3] CE04 use a systematic error of $\pm 10\,{\rm km\,s^{-1}}$ on their measured velocity of the clouds in order to derive $>2\sigma$ distance errors. We therefore adopt a $\pm 5\,{\rm km\,s^{-1}}$ 1σ velocity error for estimating the distance error to all the clouds using the Galactic rotation curve towards the line of sight presented in fig. 5 of Figer et al. (2004), based on Brand & Blitz (1993). The resulting distance errors are presented in Table 2.

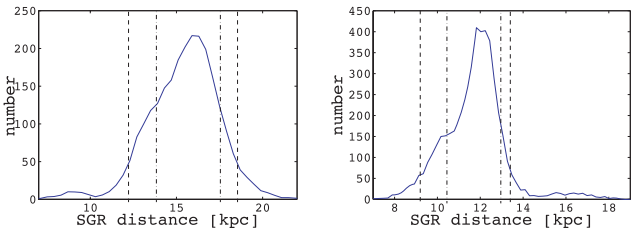

Figure 2. The distributions of the distance to SGR 1806−20 obtained by Monte Carlo simulations, with 68 and 90 per cent confidence limits marked. The left (right) distribution matches the 'near' ('far') clouds' configuration, where the three clouds with ambiguous locations are fixed at their near (far) locations (see Table 2). The best-fitting distance is $16^{+2.6}_{-3.8}$ kpc for the 'near' configuration and $11.9^{+1.6}_{-2.5}$ kpc for the 'far' configuration (90 per cent confidence).

To account for the dependence of the distance on the dust grain size distribution we run the complete procedure described above for nine different parameter choices of equation (5), with the permutations of $a_{\rm max} = 0.15,\ 0.3,\ 0.6\,\mu$m and $q = -3.5, -3, -2.5$. We find the best-fitting distance scatter due to the model choice to be smaller than the scatter due to the errors in the binned signal and in the clouds' positions and opacities [a scatter of $\sim$1 kpc between the two extreme model parameter choices, compared to $\sim$3.5 kpc (1σ) scatter due to the errors]. We therefore set the intermediate values of $a_{\rm max} = 0.3\,\mu$m and $q = -3$ as our model parameters for the analysis. In Section 4.2 we measure q and find a lower limit for $a_{\rm max}$, which are consistent with the parameters we choose for this analysis, and the errors in which are consistent with the range we use for this parameter independency check. The absence of a measured upper limit for $a_{\rm max}$ has no influence on this analysis since the dominant clouds fall within the power-law regime (see equation 4) for any $a_{\rm max}$ bigger than the value chosen here.

The effect of the SGR position on the scattered signal and on the fit quality is demonstrated in Fig. 3. For an SGR at 16 kpc, the clouds' concentrations at 4.5 and 6 kpc nearly merge, overlapping with the measured signal, while the 3-kpc clouds are negligible. In contrast, with the SGR at 6 kpc the clouds' concentrations are more separated, with the dominant 4.5 kpc cloud and the measured signal largely unsynchronized. For the 'near' configuration, the best-fitting distance is $16^{+2.6}_{-3.8}$ kpc (90 per cent confidence), with χ^2/d.o.f. = 43.3/47. For the 'far' configuration, the best-fitting distance is $11.9^{+1.6}_{-2.5}$ kpc (90 per cent confidence) with χ^2/d.o.f. = 45.9/47. Since the goodness of fit for both the configurations is similar, we use their combination to set conservative limits, with a lower limit of 9.4 kpc and an upper limit of 18.6 kpc on the distance to SGR 1806−20 at a 90 per cent confidence level.

We note that taking the main bulk of the dust along the line of sight according to CE04, concentrated at 4.5 kpc, and substituting in equation (1) with our observed ring's θ and t, results in a distance of 15 kpc for SGR 1806−20. Our above analysis wraps this crude estimation with the confidence limits permitted by the XRT observations and the CE04 errors.

The weakest link of our analysis is the accuracy of the clouds' locations as reported in CE04. For an example, Figer et al. (2004) suggested, based on a different method for measuring the radial velocity, a distance of 11.8 kpc (versus 15.1 ± 0.9 of CE04) to cloud MC13A. Although this cloud has a minor influence on our analysis, the discrepancy in this measurement demonstrates the limitation of our method. However, the goodness of fit we obtain, χ^2/d.o.f. $\approx$ 1, provides a consistency check for the CE04 clouds' distribution along the line of sight. In Section 5 we argue that future post-burst observations could resolve the location of a few individual clouds. This would potentially permit an SGR distance estimate that depends, independently, on the location of each of the resolved clouds, thereby resulting in a more robust and accurate distance measurement for this SGR.

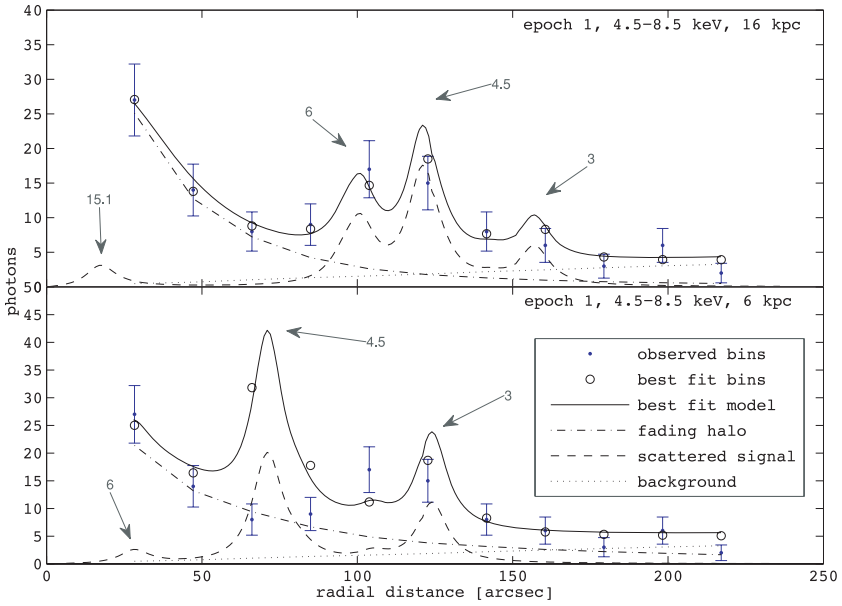

Figure 3. A comparison of the best-fitting χ^2 obtained for SGR 1806−20 located at 6 kpc versus 16 kpc, with clouds at the 'near' clouds' configuration (see Table 2). Circles mark the best-fitting model binnned photon counts while dots with error bars (Poisson, 1σ) mark the measured bin photon counts. Arrows indicate the positions in kpc of the main clouds' concentrations corresponding to each peak. An SGR distance of 16 kpc evidently provides a good fit to the data, while a distance of 6 kpc is ruled out at a $>3\sigma$ level. Model components: dotted line is the background, dotted–dashed is the fading halo, dashed is the calculated signal profile, continuous line is sum of the three components of the best-fitting model.

4.2 Constraints on dust properties

Here we assume a single predominant dust screen at an unknown a priori location, thus rejecting our previous reliance on the CE04 results. This assumption is motivated by the fact that the XRT observations show a single ring. Fitting the observed radial profile fluxes and photon energies using equation (5), we obtain best-fitting values for $\hat{a}_{\rm max}$, q and $B(E)$. Since $\hat{a}_{\rm max} = a_{\rm max}/(1-x)$ the fit results in a joint constraint on $a_{\rm max}$ and x. Therefore, the dust screen relative location, x, cannot be constrained without prior knowledge on $a_{\rm max}$, and vice versa. The model we use assumes a power-law grain size distribution, $N_{\rm a} \propto a^q$, with a grain size of $a_{\rm min} < a < a_{\rm max}$, leading to the three scattered flux regimes described in equation (8). Thus, constraining q requires observations at epochs or angles within the power-law regime, while constraining $\hat{a}_{\rm max}$ requires further inclusion of earlier observations, towards the constant flux asymptote.

Fitting the observations to the dust model is done in two steps. First we find the integrated scattered signal flux within the ring and its associated flux probability distribution (from simulations) per epoch (for the four epochs in Table 1) per energy band by fitting the observed data to a model. Then we use these fluxes as a function of epoch and energy, and their probability distributions, to obtain best-fitting values for $\hat{a}_{\rm max}$, q and $B(E)$ by means of a maximum likelihood fit using equation (5).

We model the dust-scattered signal as a Gaussian profile, thus accounting for *Swift* PSF and exposure duration effect, assuming that the effect of the clouds' width is negligible. In order to calculate the scattered signal net flux per energy band per epoch, we fit each observed radial profile to a model composed of the following three components: (a) the Gaussian profile representing the scattered signal; (b) the measured background profile; and (c) the halo around the SGR described in Section 2. The contribution of each component to each bin is weighted according to the bin's average exposure time due to the exposure maps. We run a minimum χ^2 fit with the fading halo amplitude and power, and the Gaussian amplitude and width as the free parameters. For the first observation we also fit for the radius of the Gaussian centre and obtain[4] $\theta = 119 \pm 5$ arcsec (2σ). We fix the ring location of the other observations using $\theta\,(t) \propto \sqrt{t}$ (equation 1). Fig. 4 shows the best-fitting model for the first two epochs. The best-fitting Gaussian area translates into the photon count per second related to the scattered signal, which we convert to flux using NASA's HEASARC web-based tool WebPIMMS.[5]

We find the probability distribution of each ring's integrated flux by Monte Carlo simulations. The best-fitting radial profile from the χ^2 fit is used as the base data set for preparing (assuming Poisson distribution for the bins photon count) 5000 binned profile realizations. Collecting the best-fitting flux of each realization we compile the flux probability distribution.

These distributions are then used as the input for a maximum likelihood fit, where we find the best-fitting values for $\hat{a}_{\rm max}$ and q, along with two normalization factors B_E, one per energy band. For a given set of parameters $\hat{a}_{\rm max}$, q and $B(E)$, we use equation (5) to calculate the flux at each observation epoch and energy band. We then evaluate the likelihood of this set using the measured flux distribution. The set of parameter values which yields the highest product of likelihoods for all epochs and energy bands is the best fit. Fig. 5 shows the 1σ bars of the flux distributions, and the corresponding best-fitting model.

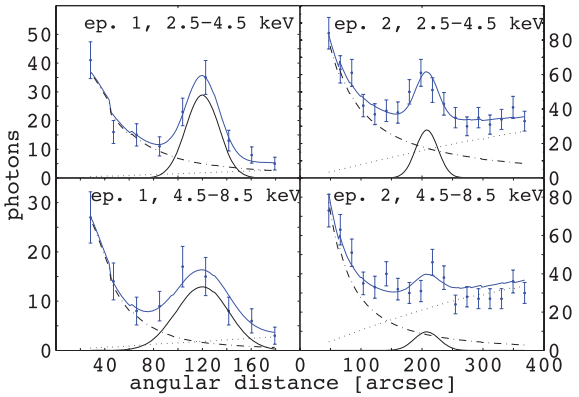

Figure 4. χ^2 fits for the first two epochs in the two energy bands. The dotted line is background, dotted–dashed is the fading halo, the bottom continuous line is the scattered signal Gaussian and the top line is the sum of the three components. Dots with error bars (Poisson, 1σ) are the binned measured photon counts. The best-fitting Gaussian area translates into the flux per epoch and energy band (Table 3), flux errors distribution are found using Monte Carlo simulations (see text).

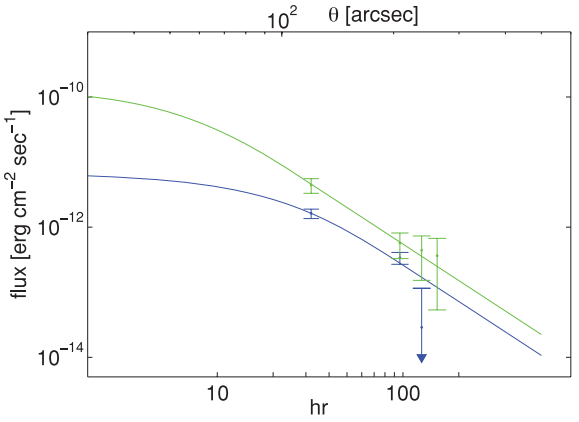

Figure 5. Maximum likelihood best-fitting model (equation 5). The lower line and the accompanying dots and error bars (Table 3) are the 2.5–4.5 keV band. The best-fitting result for the power-law index q is $-3.3^{+0.6}_{-0.7}$ (1σ), with errors determined from Monte Carlo simulations. The best-fitting result for $\hat{a}_{\rm max} = a_{\rm max}/(1-x)$ is 0.33 μm. Since the first observation is almost completely within the flux power-law regime (see equation 8), we cannot set an upper limit for $\hat{a}_{\rm max}$. The 2σ lower limit is 0.21 μm (see Fig. 6).

Estimation of the confidence limits of these parameters is calculated by Monte Carlo simulations. For each Monte Carlo run we generate a realization of the fluxes in Table 3, with the ring's integrated flux values drawn from the actual best-fitting distribution in Table 3. The errors around the drawn flux values are taken to be the same as the original errors in Table 3. We fit 5000 Monte Carlo realizations for $\hat{a}_{\rm max}$, q and $B(E)$, thus obtaining the probability distribution of these parameters.

Fluxes used for the maximum likelihood fit, with 1σ errors and χ^2 values, are listed in Table 1. The best-fitting result for q is $-3.3^{+0.6}_{-0.7}$ (1σ), consistent with the commonly cited -3.5 from Mathis et al. (1977) and with an implicit -3 of Draine (2003). The best-fitting result for $\hat{a}_{\rm max}$ is 0.33 μm. As indicated by the likelihood contours of q and $\hat{a}_{\rm max}$ shown in Fig. 6, we are unable to constrain $\hat{a}_{\rm max}$ from above, which is the result of the earliest observation being too

[4] An upper limit of 6.37 kpc for the dominant dust screen, regardless of the source position, is obtained by substituting the observed ring's θ and t in equation (1) (a 6.6-kpc upper limit was reported by Goad et al. 2006).

[5] Using a power-law source model with photon index -1, i.e. a blackbody Rayleigh–Jeans law (e.g. Feroci et al. 2004), and $N_{\rm H} = 6 \times 10^{22}\,{\rm cm}^{-2}$ (Sonobe et al. 1994).

Table 3. Best-fitting ring's integrated fluxes used for the maximum likelihood fit.

Epoch	Time since burst (h)	Energy band (keV)	Flux (erg cm^{-2} s^{-1})	χ^2/d.o.f.
1	30.8	2.5–4.5	$1.63 \pm 0.27 \times 10^{-12}$	2.95/4
1	30.8	4.5–8.5	$4.45 \pm 1.13 \times 10^{-12}$	2.00/5
2	93.5	2.5–4.5	$3.39 \pm 0.71 \times 10^{-13}$	6.15/15
2	93.5	4.5–8.5	$5.73 \pm 2.45 \times 10^{-13}$	17.25/15
3	121.1	2.5–4.5	$2.88 \pm 8.70 \times 10^{-14}$	7.59/11
3	121.1	4.5–8.5	$4.43 \pm 2.92 \times 10^{-13}$	13.31/11
4	147.6	4.5–8.5	$3.64 \pm 3.12 \times 10^{-13}$	16.83/11

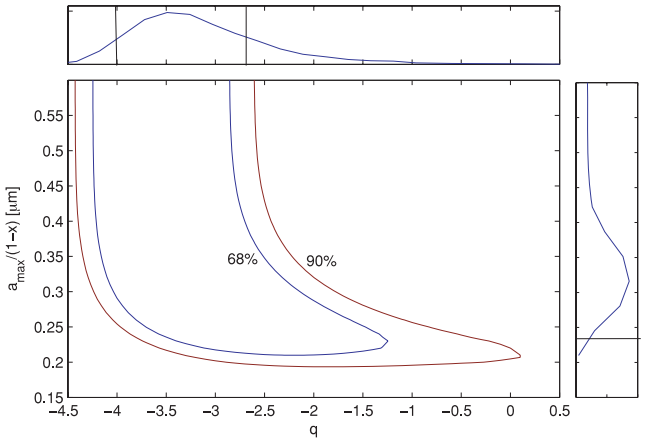

Figure 6. 68 and 90 per cent likelihood contours of q and $\hat{a}_{\max}$ as determined from the Monte Carlo simulations. Note the lack of an upper limit for $\hat{a}_{\max}$. The marginalized distribution of each parameter is shown above (q) and to the right ($\hat{a}_{\max}$). The lines mark the 68 per cent confidence limits for each single parameter, based on an integration of the probabilities for $\hat{a}_{\max} \leq 3$ μm.

adjacent to the power-law asymptote regime (see Fig. 5). We thus find only a lower limit of 0.21 μm (2σ) for $\hat{a}_{\max}$.

In our fit we constrain $\hat{a}_{\max}$, which is a combination of $a_{\max}$ and x ($\hat{a}_{\max} \equiv \frac{a_{\max}}{1-x}$). In order to learn further about either x or $a_{\max}$ one needs to have prior knowledge of either $a_{\max}$ or x, respectively. Since $\theta(t)$ is known, a measurement of x will provide an SGR distance estimate that is independent of our previous analysis. However, prior constraints on the distance to SGR 1806−20, 6–15 kpc (Section 1), translate, together with the locations of the ring, into $0.30 < x < 0.51$ (equation 1). Therefore, improving these constraints on x requires constraints on both $\hat{a}_{\max}$ and $a_{\max}$ that are better than 25 per cent. The uncertainty in the value of $\hat{a}_{\max}$ in the diffused ISM is larger, while its value in molecular clouds is practically unknown. Therefore, our measured $\hat{a}_{\max}$, and even an ideal errorless $\hat{a}_{\max}$, are useless for improving the constraints on the distance to SGR 1806−20. This conclusion is similar to that of Tiengo et al. (2010), who found that the distance to the X-ray pulsar 1E1547.0–5408 cannot be conclusively determined due to the uncertainty in the dust properties, although they obtained superb data.

In the case of SGR 1806−20, however, there are robust (although rather loose) limits on its distance. Thus, the prior constraints on x can be used to efficiently constrain $a_{\max}$, which is of special interest in our case of molecular clouds. The robust constraint of $d > 6$ kpc for the SGR's distance (Cameron et al. 2005) matches $x < 0.51$, which translates into $a_{\max} > 0.1$ μm (2σ).

The best-fitting results for the normalization factors are $B(2.5\text{–}4.5\text{keV}) = 2.89^{+0.86}_{-0.81} \times 10^{-13}$ erg cm^{-2} s^{-1} arcsec^{-2}, $B(4.5\text{–}8.5\text{keV}) = 6.10^{+1.27}_{-1.21} \times 10^{-12}$ erg cm^{-2} s^{-1} arcsec^{-2}. As a consistency check, we use the ratio between the two normalization constants to find the hydrogen column density towards SGR 1806−20. The normalization constant depends on photon energy through S_E, the directly observed fluence. Given the source spectrum and the X-ray extinction cross-section per H nucleon per energy $\sigma(E)$, $N_{\rm H}$ can be extracted using $S_E \propto \exp\{-\sigma(E)N_{\rm H}\}$. Assuming that the X-ray extinction is mainly dust driven, we take the X-ray extinction cross-section per H nucleon due to dust for each energy band from Draine (2003) (assuming $R_V = 3.1$). For the burst X-ray spectrum at our energy bands we follow Feroci et al. (2004) and Olive et al. (2003) in adopting a double blackbody spectrum instead of the OTTB spectrum commonly used to describe SGR bursts in the range of 20–200 keV (e.g. Golenetskii et al. 2005). Using the average double blackbody spectrum of $kT_1 = 3.4, kT_2 = 9.3, L_1/L_2 = 0.85$ from Feroci et al. (2004) with our best-fitting ratio, we get $N_{\rm H} = 9.64^{+2.8}_{-4.0} \times 10^{22}$ cm^{-2}, consistent with Sonobe et al. (1994).

Reversing the last procedure we find the normalizations ratio between the 2.5–4.5 keV band and the 0.5–2.5 keV band, which we did not use due to a lack of signal, to be 1000:1, explaining the lack of signal beyond the background noise in the 0.5–2.5 keV energy band.

5 FUTURE SGR OBSERVATIONS

The accuracy of the derived distance to SGR 1806−20 and the properties of the dust along the line of sight are restricted by large error bars due to the weak signal and low resolution of the *Swift*/XRT, and by the long delay between the burst and the first echo observation. Nevertheless, our analyses demonstrate the wealth of information that can be extracted from observing dust-scattered X-ray echoes of bursts. Encouraged by these results, we provide guidelines for optimal future observations of magnetar bursts, showing that improved observations' timing, resolution and sensitivity would yield far better constraints on both the distance to an SGR and the properties of the intervening dust.

In order to evaluate the expected angular scattered width of the ring we compare the effects of the clouds' width, exposure duration and PSF. Substituting an SGR distance of 15 kpc and $x = 0.3$ (i.e. main cloud at 4.5 kpc) in equation (1) we get a spread of roughly 1 arcsec for an assumed typical cloud width of 100 pc, and a spread of $\Delta\theta = 0.36\,\text{arcsec}(t_{\rm start}^{1/2} - t_{\rm end}^{1/2})$ due to exposure duration (where t is the time passed in seconds since the direct observation of the burst). This yields a width of ∼1 arcsec for the first XRT epoch, at a delay of 30 h and duration of 40 min, due to the non-PSF effects. Thus the width is practically set by the PSF of the telescope, with ∼20 arcsec for *Swift*/XRT versus 1 arcsec for *Chandra*.

Effective constraining of $a_{\max}$ requires making observations earlier than 30 h after the burst, and such a response time is suitable for *Swift*/XRT. With a stronger scattered signal and a sharper decay of the King component for earlier observations, resolving the scattered signal from the source should be possible for a ∼1 h observation taken 12 h after the burst ($\theta_{\rm obs} = 75$ arcsec). Since observations should also cover the scattered flux power-law regime, the burst fluence should be similar or larger than the 2006 August 6 burst.

Chandra observation can be obtained with a response time of a few days. The improved resolution and collection area of *Chandra* could significantly reduce errors and improve statistics. *Chandra* also enables a continuous observation due to its high orbit, thus minimizing the spread due to exposure duration. A resolution of

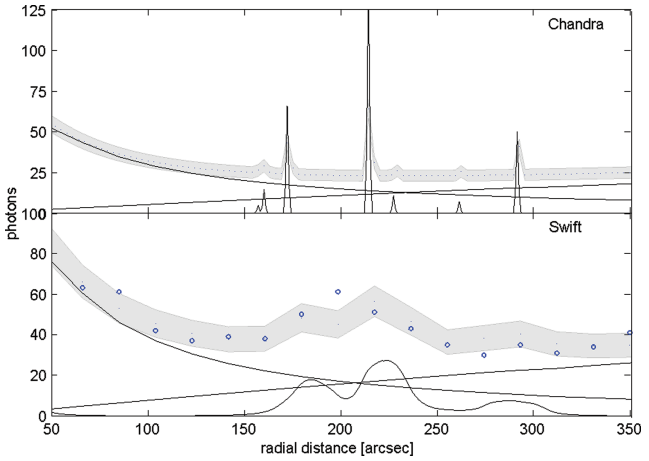

Figure 7. A comparison of the best-fitting photon counts for the second epoch 2.5–4.5 keV band with SGR at 16 kpc, *Swift* versus *Chandra*. Based on a *Chandra* four-fold signal and 3 arcsec resolution. Contributions of the clouds' scattered signal, background and fading halo are shown as continuous lines. Poisson 1σ confidence limits for the best-fitting photon counts are marked as grey filled area. *Swift* actual measured photon counts are marked with circles.

2–3 arcsec (accounting for PSF, exposure duration and cloud width) and a signal roughly four times that of *Swift* should improve the signal-to-noise ratio, and enable resolving the location of individual clouds along the line of sight. Each of the resolved clouds will provide an independent constraint on the SGR distance. This will provide a more accurate and, more importantly, a more robust distance estimate. In Fig. 7 we illustrate the advantages of using *Chandra*, comparing what *Chandra* would have seen at the second XRT epoch to the actual *Swift* observation.

The burst energy determines the proper time for the last effective observation. A delay of 30 h, equivalent to $\theta = 120$ arcsec, is located within the power-law regime flux decay (equation 8), as seen in Fig. 5. Using our $q = -3.3$, combined with our measured scattered flux, we obtain

$$F_{\rm scat} = F_0 \frac{\Phi}{\Phi_{\rm 2006\ August\ 6}} \left(\frac{t_{\rm delay}}{30\,{\rm hr}}\right)^{-1.85}, \qquad (10)$$

where Φ is the measured event fluence and $F_0(2.5\text{–}4.5\,{\rm keV}) = 1.63 \times 10^{-12}\,{\rm erg\,cm^{-2}\,s^{-1}}$ and $F_0(4.5\text{–}8.5\,{\rm keV}) = 4.45 \times 10^{-12}\,{\rm erg\,cm^{-2}\,s^{-1}}$ are the fluxes from Table 3. The equation is valid for $t_{\rm delay} \geqslant 30$ h (power-law regime). We calibrate the background photon count by the total background photon count measured for *Swift* (e.g. 0.14 photons $\rm s^{-1}$ for 2.5–4.5 keV), with the background per radial bin piling up as $\theta \propto \sqrt{t}$. By requiring that the bin that contains the largest fraction $f \leq 1$ of the scattered signal be N_σ times larger than the background error, we get a rough estimate of the maximum delay for an effective observation:

$$t = t_0 \left(\frac{\Phi}{\Phi_{\rm 2006\ August\ 6}} \frac{5}{N_\sigma} f \sqrt{\frac{10\,{\rm arcsec}}{\rm binwidth} \frac{A_{\rm eff}}{A_{\rm eff}^{\rm Swift}} \frac{\Delta t}{1\,{\rm hr}}}\right)^{0.48}, \qquad (11)$$

where $t_0(2.5\text{–}4.5\,{\rm keV}) = 135$ h and $t_0(4.5\text{–}8.5\,{\rm keV}) = 120$ h; $A_{\rm eff}$ is the detector's effective area for the chosen energy band; and Δt is the observation's exposure time in hours.

For the *Swift* case at 2.5–4.5 keV we get a $>5\sigma$ detection for the first observation, at $t = 30$ h, and a $\sim 5\sigma$ detection for the $t = 100$ h second observation. A *Chandra* $A_{\rm eff} \approx 4A_{\rm eff}^{\rm Swift}$, $\Delta t = 5$ h (for the latest observation), a binwidth of 3 arcsec and $f \approx 1$ permits a 5σ detection for as long as 370 h after a burst of the same fluence, thus probing dust grains down to a size of $\sim 0.022\,\mu$m (versus $\sim 0.035\,\mu$m in our case). Alternatively, a *Chandra* observation of $\Delta t = 3$ h after 100 h can yield a 5σ detection for a burst of a fluence 10 times weaker than that of 2006 August 6. Such SGR bursts are more common, offering more opportunities for observations.

Equations (10) and (11) quote the fluence of the 2006 August 6 burst. The measured event fluence in the range of 20–200 keV is $\Phi = 2.4 \times 10^{-4}\,{\rm erg\,cm^{-2}}$ (Golenetskii et al. 2006). We assume, at least for minor/intermediate bursts, a similar spectrum across different energy outputs (e.g. Olive et al. 2003; Feroci et al. 2004). Hence, for events for which the fluence is given at 20–200 keV, one should substitute the above-cited fluence by the new event fluence. For events where the band fluence (e.g. 2.5–4.5 keV) is more accessible, or events for which the similar spectrum assumption does not necessarily hold (e.g. giant flares), we supply an estimate of the 2006 August 6 burst fluence at the 2.5–4.5 keV and the 4.5–8.5 keV energy bands. Olive et al. (2004), Feroci et al. (2004), Nakagawa et al. (2007) and Israel et al. (2008) obtain satisfying fits for the spectra of minor/intermediate SGR bursts using models composed of two blackbody components, a harder one ($kT \approx$ 9–10) and a softer one ($kT \approx$ 3–4). Israel et al. (2008) compared three of the cited works and found the bolometric luminosities of the two components to be similar, with a possible saturation of the soft component above $10^{41}\,{\rm erg\,s^{-1}}$. We adopt an equal luminosity for both the components. Calibrating all the cited models with the SGR fluence per keV at $kT = 20$ (derived from the total measured fluence and an OTTB spectrum of $kT = 20$ keV over the range of 20–200 keV), we calculate the band fluence according to the blackbody temperatures of each cited model, and estimate the fluence as the geometric mean of the two extreme model results, obtaining $\Phi_{2.5\text{–}4.5} = 9.3^{+6.0}_{-3.6} \times 10^{-6}\,{\rm erg\,cm^{-2}}$ and $\Phi_{4.5\text{–}8.5} = 4.1^{+2.0}_{-1.4} \times 10^{-5}\,{\rm erg\,cm^{-2}}$. These values can be used for equations (10) and (11) along with the respective band fluence of a new event, regardless of the event's spectrum.

A burst brighter than the one we analysed should enable probing smaller dust grains and even, if bright enough, allow the determination of $a_{\rm min}$, the lower cut-off of the dust grain size distribution. The launch of *NuSTAR* next year may provide an opportunity to constrain $a_{\rm min}$ by observing echoes from an intermediate burst, since for a given $a_{\rm min}$ the transition time from the power-law regime to the exponential decay regime is proportional to θ^2 and therefore to E^{-2} (equation 4). *NuSTAR* has a sensitivity range of 5–80 keV and a larger effective area compared to *Chandra* (for $E < 35$ keV). In addition, the signal-to-noise ratio at higher energies should improve due to the spectrum of SGR bursts and to the decrease in the background level. On the other hand, *NuSTAR's* relatively low resolution of 43 arcsec will dilute the signal. Taking it all into account, *NuSTAR* should be able to follow hard X-ray echoes from intermediate bursts for a few days after the burst, thus probing much smaller grains, and potentially identifying $a_{\rm min}$.

Generally, X-ray echoes observations taken during different bursts of the same SGR can be combined to improve the signal-to-noise ratio and thus improve the constraints discussed in this work.

6 CONCLUSIONS

We used *Swift*/XRT observations following an intermediate burst of SGR 1806−20 to constrain the distance to the SGR and to find the first X-ray echo constraints on molecular clouds' dust properties. Based on the molecular clouds' properties along the line of sight

found by CE04 and the observed echoes of the burst we constrain the distance with a lower limit of 9.4 kpc and an upper limits of 18.6 kpc at a 90 per cent confidence level. This upper limit can be considered the first direct upper limit set for the distance to the SGR, as the upper limit set by Cameron et al. (2005) is questionable, and other distance estimates are based on association rather than measured emission from the source. Our distance constraints favour an energy output of $\sim 10^{46}$ erg s^{-1} for the 2004 giant flare of SGR 1806−20, leaving Galactic versus extragalactic giant burst rate's possible tension and the lack of post-burst emission features changes in SGR 1806−20 as open issues.

We introduce the use of observations of dust X-ray echoes for probing the dust properties of molecular clouds. Fitting the spectral and temporal signal evolution using a dust-scattering model with an assumed power-law dust grain size distribution, we find a power-law index of $q = -3.3^{+0.6}_{-0.7}$ (1σ) and that the dust maximal grain size $a_{\max} > 0.1$ μm (2σ). These results are of special interest since the dust along the line of sight to SGR 1806−20 resides in molecular clouds, which points at such dust properties that have been poorly explored so far. The constraints we have obtained imply that the dust grain size distribution in molecular clouds may be similar to the one found in diffused ISM (e.g. Mathis et al. 1977).

The wealth of data obtained using *Swift*/XRT encourage us to suggest the use of future X-ray echoes observations. For an intermediate SGR 1806−20 burst, a *Swift* observation starting half a day after the burst and a *Chandra* observation a few days after the burst should yield superior dust grain size distribution characterization and SGR distance constraints, respectively. A *Chandra* observation should enable, in addition, a quality mapping of clouds' locations along the line of sight. *NuSTAR*, planned to be launched in 2112, could potentially probe $a_{\min}$, the minimal dust grain size.

The authors would like to thank Bruce Draine, Eli Dwek, Derek Fox and Amiel Sternberg for helpful discussions. Special thanks to Chryssa Kouveliotou for helpful comments and careful reading of the manuscript. This work was partially supported by the Israel Science Foundation (grant No. 174/08) and by an IRG grant. EOO is supported by an Einstein fellowship and NASA grants.

REFERENCES

Bibby J. L., Crowther P. A., Furness J. P., Clark J. S., 2008, MNRAS, 386, L23
Brand J., Blitz L., 1993, A&A, 275, 67
Burrows D. N. et al., 2005, Space Sci. Rev., 120, 165
Butler M. J., Tan J. C., 2009, ApJ, 696, 484
Cameron P. B. et al., 2005, Nat, 434, 1112
Carrasco L., Strom S. E., Strom K. M., 1973, ApJ, 182, 95
Chiar J. E. et al., 2007, ApJ, 666, L73
Corbel S., Eikenberry S. S., 2004, A&A, 419, 191 (CE04)
Draine B. T., 2003, ApJ, 598, 1026
Duncan R. C., Thompson C., 1992, ApJ, 392, L9
Esposito P. et al., 2007, A&A, 476, 321
Feng L., Fox D. B., 2010, MNRAS, 404, 1018
Feroci M., Caliandro G. A., Massaro E., Mereghetti S., Woods P. M., 2004, ApJ, 612, 408
Figer D. F., Najarro F., Kudritzki R. P., 2004, ApJ, 610, L109
Figer D. F., Najarro F., Geballe T. R., Blum R. D., Kudritzki R. P., 2005, ApJ, 622, L49
Goad M. R., Page K. L., Godet O., O'Brien P. T., Vaughan S., Hurley K., 2006, GRB Coordinates Network, 5438, 1
Göğüş E., Kouveliotou C., Woods P. M., Finger M. H., van der Klis M., 2004, Nuclear Phys. B, 132, 604
Goldsmith P. F., Bergin E. A., Lis D. C., 1997, ApJ, 491, 615
Golenetskii S. et al., 2005, GRB Coordinates Network, 4312, 1
Golenetskii S., Frederiks D., Pal'Shin V., Aptekar R., Cline T., Mazets E., 2006, GRB Coordinates Network, 5426, 1
Hurley K. et al., 2005, Nat, 434, 1098
Hurley K. et al., 2006a, GRB Coordinates Network, 5419, 1
Hurley K. et al., 2006b, GRB Coordinates Network, 5416, 1
Israel G. L. et al., 2008, ApJ, 685, 1114
Jura M., 1980, ApJ, 235, 63
Kouveliotou C., 1998, BAAS, 30, 1332
Kouveliotou C. et al., 1998, Nat, 393, 235
Kouveliotou C. et al., 2001, ApJ, 558, L47
Mathis J. S., Rumpl W., Nordsieck K. H., 1977, ApJ, 217, 425
Mauche C. W., Gorenstein P., 1986, ApJ, 302, 371
Mazets E. P., Golenetskii S. V., 1981, Ap&SS, 75, 47
McClure-Griffiths N. M., Gaensler B. M., 2005, ApJ, 630, L161
Moretti A. et al., 2005, in Siegmund O. H. W., ed., Proc. SPIE Vol. 5898, UV, X-Ray, and Gamma-Ray Space Instrumentation for Astronomy XIV. SPIE, Bellingham, p. 348
Nakagawa Y. E. et al., 2007, PASJ, 59, 653
Nakar E., Gal-Yam A., Piran T., Fox D. B., 2006, ApJ, 640, 849
Ofek E. O., 2007, ApJ, 659, 339
Olive J. et al., 2003, in Ricker G. R., Vanderspek R. K., eds, AIP Conf. Ser. Vol. 662, Gamma-ray Burst and Afterglow Astronomy 2001: A Workshop Celebrating the First Year of the HETE Mission. Am. Inst. Phys., Melville, NY, p. 82
Olive J. et al., 2004, ApJ, 616, 1148
Ormel C. W., Paszun D., Dominik C., Tielens A. G. G. M., 2009, A&A, 502, 845
Ossenkopf V., 1993, A&A, 280, 617
Overbeck J. W., 1965, ApJ, 141, 864
Paczynski B., 1992, Acta Astron., 42, 145
Palmer D. M. et al., 2005, Nat, 434, 1107
Predehl P., Schmitt J. H. M. M., 1995, A&A, 293, 889
Predehl P., Burwitz V., Paerels F., Trümper J., 2000, A&A, 357, L25
Press W. H., Flannery B. P., Teukolsky S. A., 1986, in Press W. H., Flannery B. P., Teukolsky S. A., eds, Numerical Recipes: The Art of Scientific Computing. Cambridge Univ. Press, Cambridge
Rivera Ingraham A., van Kerkwijk M. H., 2010, ApJ, 710, 797
Schnee S., Li J., Goodman A. A., Sargent A. I., 2008, ApJ, 684, 1228
Smith R. K., Dwek E., 1998, ApJ, 503, 831
Sonobe T., Murakami T., Kulkarni S. R., Aoki T., Yoshida A., 1994, ApJ, 436, L23
Stepnik B. et al., 2003, A&A, 398, 551
Tiengo A. et al., 2010, ApJ, 710, 227
Trümper J., Schönfelder V., 1973, A&A, 25, 445
van de Hulst H. C., 1957, in van de Hulst H. C., ed., Light Scattering by Small Particles
Vianello G., Tiengo A., Mereghetti S., 2007, A&A, 473, 423
Weidenschilling S. J., Ruzmaikina T. V., 1994, ApJ, 430, 713
Winston E. et al., 2007, ApJ, 669, 493
Woods P. M., Thompson C., 2006, in Lewin W. H. G., van der Klis M., eds, Compact Stellar X-ray Sources. Cambridge Univ. Press, Cambridge, p. 547
Woods P. M., Kouveliotou C., Finger M. H., Göğüş E., Wilson C. A., Patel S. K., Hurley K., Swank J. H., 2007, ApJ, 654, 470

This paper has been typeset from a TEX/LATEX file prepared by the author.